

PCCP

Toxic, Radioactive, and Disordered: A Total Scattering Study of TITcO4

Journal:	Physical Chemistry Chemical Physics		
Manuscript ID	CP-ART-09-2024-003707.R1		
Article Type:	Paper		
Date Submitted by the Author:	1 11-1007-20124		
Complete List of Authors:	Mullens, Bryce G.; The University of Sydney Marlton, Frederick; UTS, Mathematical and physical science Saura-Múzquiz, Matilde; The University of Sydney, School of Chemistry; Aarhus University, Department of Chemistry & iNANO; Departamento de Física de Materiales, Facultad de Ciencias Físicas, Universidad Complutense de Madrid, 28040, Madrid, Spain Everett, Michelle; Oak Ridge National Laboratory, Spallation Neutron Source Li, Cheng; Oak Ridge National Laboratory, Materials; Imperial College London, Manjón-Sanz, Alicia; Oak Ridge National Laboratory Tucker, Matthew; Oak Ridge National Laboratory Louis-Jean, James; University of Nevada Las Vegas College of Sciences, Department of Chemistry and Biochemistry Poineau, Frederic; University of Nevada Las Vegas, Department of Chemistry Mukherjee, Supratik; Advanced Center of Research in High Energy Materials (ACRHEM), University of Hyderabad, Physics Mondal, Subrata; University of Hyderabad Advanced Centre of Research in High Energy Materials, School of Physics Vaitheeswaran, Ganapathy; University of Hyderabad Kennedy, Brendan; The University of Sydney		

SCHOLARONE™ Manuscripts

Toxic, Radioactive, and Disordered: A Total Scattering Study of TITcO₄

Bryce G. Mullens,¹ Frederick P. Marlton,^{2,*} Matilde Saura-Múzquiz,³ Michelle Everett,⁴ Cheng Li,⁴ Alicia M. Manjon-Sanz,⁴ Matthew G. Tucker,⁴ Frederic Poineau,⁵ James Louis-Jean,⁵ Supratik Mukherjee,⁶ Subrata Mondal, ⁶ Ganapathy Vaitheeswaran,^{7,*} and Brendan J. Kennedy¹

¹ School of Chemistry, The University of Sydney, Sydney, New South Wales 2006, Australia.

² Centre for Clean Energy Technology, School of Mathematical and Physical Sciences, Faculty of Science, University of Technology Sydney, Sydney, New South Wales 2007, Australia.

³ Departamento de Física de Materiales, Facultad de Ciencias Físicas, Universidad Complutense de Madrid, 28040, Madrid, Spain.

⁴ Neutron Scattering Division, Oak Ridge National Laboratory, Oak Ridge, Tennessee 37831, USA.

⁵ Department of Chemistry, University of Nevada Las Vegas, Las Vegas, Nevada, 89154, USA.

⁶ Advanced Centre of Research in High Energy Materials (ACRHEM), University of Hyderabad, Prof. C. R. Rao Road, Gachibowli, 500046 Hyderabad, Telangana, India.

⁷ School of Physics, University of Hyderabad, Prof. C. R. Rao Road, Gachibowli, 500046 Hyderabad, Telangana, India.

^{*} Corresponding Authors: Brendan J. Kennedy (brendan.kennedy@sydney.edu.au) and Ganapathy Vaitheeswaran (vaithee@uohyd.ac.in)

Abstract

A detailed variable temperature neutron total scattering study of the potential nuclear waste matrix TlTcO₄ was conducted. The long-range average structure of TlTcO₄ undergoes an orthorhombic *Pnma* to tetragonal I4₁/amd phase transition below 600 K, consistent with previous synchrotron X-ray diffraction studies. However, several anomalies were observed in the Rietveld refinements to the neutron powder diffraction data, such as large atomic displacement parameters at low temperature and a shortening of the Tc–O bond distance upon heating. Modelling the short-range local structure of both the low and high-temperature data required a lowering of symmetry to the monoclinic $P2_1/c$ model due to the stereochemical activity of the Tl⁺ 6s² lone pairs. Density functional theory calculations also verified this model to have a lower ground state energy than the corresponding long-range average structure. It is concluded that at low temperatures, the Tl^+ 6s² lone pairs are 'frozen' into the structure. Upon heating, the rigid TcO_4 tetrahedra begin to rotate, as governed by the Γ_3^+ and M_4^+ modes. However, there is a disconnect between the two length scales, with the 6s² lone pair electrons remaining stereochemically active on the local scale, as observed in the neutron pair distribution function fits. The orthorhombic Pnma to tetragonal $I4_1/amd$ phase transition is seemingly the result of a change in the correlation length of the Tl⁺ 6s² lone pairs, leading to a larger unit cell volume due to their uncorrelated displacements.

Introduction

The increasing concern of carbon emissions, in the context of climate change, has caused a global shift in the world's reliance on carbon-based fuels. This has led to a renewed interest in nuclear power which, according to the US Office of Nuclear Energy, provided almost half of the United States' carbon-neutral energy in 2023. The safe storage of fission products from spent nuclear fuel remains a major challenge and is a constant impediment to the continued use of nuclear power. One of the most challenging fission products is 99 Tc, with a cumulated yield of \sim 6% from 235 U fission. Technetium-99m (99m Tc) is currently used as a medical radioisotope for selective imaging diagnosis due to its relatively short half-life, accounting for over half of all nuclear medicine procedures. However its decay product, 99 Tc (upon decaying from 99m Tc via isomeric transition), presents an environmental challenge due to its high mobility, β - emission, and half-life of around 211 000 years.

In developing technologies for the safe storage of Tc-containing waste, it is necessary to consider the chemistry of the commonly encountered oxidation states; namely Tc^{4+} and Tc^{7+} . The Tc^{4+} oxidation state is only soluble in acidic conditions (below pH \sim 3), meaning it often precipitates out as

solid TcO₂·*n*H₂O under environmental conditions.^{2, 3} Tc⁷⁺ forms the water-soluble and highly stable pertechnetate anion TcO₄- which is much more mobile and can lead to the corrosion of Fe- and Zr-based storage containers.⁴⁻⁶ As a consequence, several materials have been investigated for storing Tc-containing waste to prevent its leaching into the environment. These storage mechanisms include metal oxides,⁷ glasses,^{8, 9} and metal-organic frameworks (MOFs).^{10, 11}

Since Tc has no stable isotopes, it is common for studies to use Re as a nonradioactive surrogate. 12-16 This is due to the predicted similarities in the chemical behaviour of Tc7+ and Re7+, which are attributed to their identical oxidation states and similar ionic radii ($Tc^{7+} = 0.37 \text{ vs. } Re^{7+} =$ 0.38 Å in tetrahedra geometry). 17 However, a growing body of literature shows that Tc7+ and Re7+ do not always act identically. Lukens et al. reported that Tc7+ is significantly more volatile than Re7+, leading to a decrease in the amount stabilised in waste glasses. 18 Gan et al. described the different behaviours of Tc and Re under various redox conditions, reflecting the lower standard reduction potential of Re^{7+} ($ReO_4^{-}/ReO_2 = 0.510 \text{ V}$) compared to Tc^{7+} ($TcO_4^{-}/TcO_2 = 0.738 \text{ V}$). ¹⁹ These subtle differences are also evident in other oxides. For example, the perovskites CaTcO₃ and SrTcO₃ have exceptional magnetic properties, but their AReO₃ analogues have yet to be synthesised.²⁰⁻²² This suggests that differences in the electronic structures between the two cations may be important. Re has more radially-extended 5d valence orbitals than the 4d valence orbitals in Tc, potentially impacting its reactivity and redox stability.²³ Similar differences have also been observed in other 4d and 5d metal oxides, where the more radially-extended 5d orbitals of Ta⁵⁺ lead to more covalent character in Ta–O bonds compared to Nb-O,24 and the lighter MoO4 tetrahedra undergo a greater amount of rotational disorder compared to the heavier WO₄ analogues.²⁵

Pertechnetate salts of the type $A\text{TcO}_4$ ($A^+ = \text{NH}_4$, K, Cs) were among the first Tc oxides isolated and studied. Subsequently, several powder diffraction and single crystal studies have reported the structures and phase transitions in $A\text{TcO}_4$ and $A\text{ReO}_4$ salts. Showed that most are isostructural at room temperature. Showed that most are isostructural at room temperature. For both Tc and Re, the structures of the four salts ($A^+ = \text{Na}$, K, Rb, Ag) were refined to the CaWO₄, tetragonal scheelite, structure (space group $I4_1/a$, \$488). In this structure, the AO_8 dodecahedra contain two distinct A-O distances, whereas the BO_4 tetrahedra possess a single B-O distance (see Figure 1). The BO_4 tetrahedra are isolated from each other and connected to the AO_8 dodecahedra via bridging oxygen anions. Bastide showed that the structures of various ABO_4 compounds can be predicted from the r_A/r_O and r_B/r_O ratios, where r_X is the ionic radii of the A- and B-site cations and oxygen anion, respectively. This explains why the $ATcO_4$ and $AReO_4$ salts mostly exhibit the same room temperature structure ($r_{Tc}/r_O \sim r_{Re}/r_O$), as well as

explaining why RbTcO₄ and RbReO₄ ($r_{Rb}/r_O \sim 1.13$) exhibit the tetragonal $I4_1/a$ scheelite-type structure whilst the CsTcO₄ and CsReO₄ ($r_{Cs}/r_O \sim 1.23$) analogues exhibit an orthorhombic pseudo-scheelite structure (space group Pnma, #62. See Figure 1 and Figure S1).^{28, 30, 32-34, 36, 37} Exceptions to these ionic radii rules have been observed, as reflected in the rich structural chemistry of the LnTaO₄ (Ln^{3+} = lanthanoid La-Lu) oxides that is not replicated in the corresponding LnNbO₄ oxides.³⁸⁻⁴³

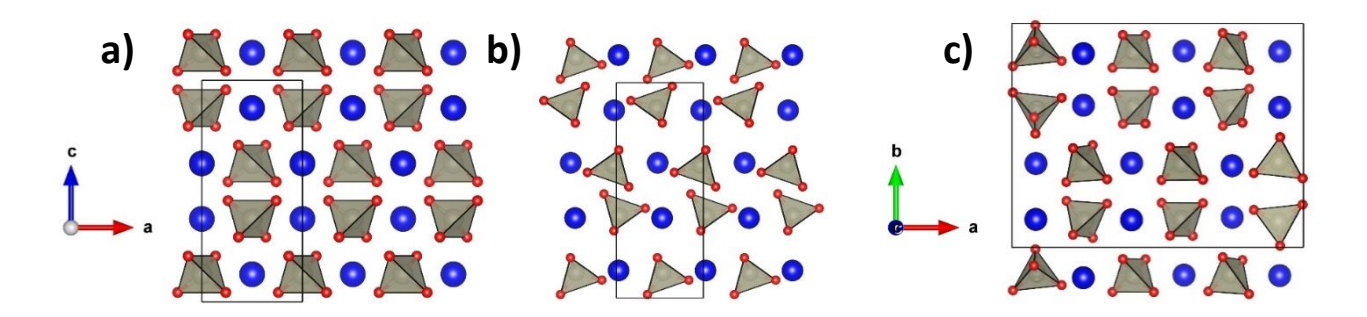


Figure 1: Crystal structures of the scheelite-type oxides for (a) tetragonal $I4_1/a$, (b) orthorhombic Pnma, and (c) monoclinic $P2_1/c$. Note that the monoclinic $P2_1/c$ unit cell has been tripled along the a axis.

Although Re⁷⁺ and Tc⁷⁺ are similar in size, previous studies have described differences between the ATcO₄ and AReO₄ salts. Reynolds *et al.* highlighted differences in the thermal behaviour between NH₄TcO₄ and NH₄ReO₄ attributed to subtle differences in the B-O (B^{7+} = Tc, Re) bonds within the BO₄ tetrahedra. More dramatic differences are evident in the two thallium salts TlTcO₄ and TlReO₄. The former adopts the orthorhombic Pnma pseudo-scheelite structure at room temperature, whereas TlReO₄ exhibits a monoclinic $P2_1/c$ (space group #14) structure (Figure 1). At The temperature dependence of the two structures is also different, with TlReO₄ exhibiting an unusual re-entrant phase transition. At a neutron total scattering study by Saura-Múzquiz *et al.* revealed that the local structure of TlReO₄ was *always* best fit to the monoclinic $P2_1/c$ space group, irrespective of the long-range average structure, with a change in the correlation length of the Tl+ 6s² lone pairs used to explain the re-entrant phase transition. This behaviour appears to be unique to TlReO₄ and has not been reported in the closely related oxide TlTcO₄ that undergoes an orthorhombic-to-tetragonal phase transition upon heating.

In this work, the temperature dependence of the structure of $TITcO_4$ was investigated using neutron total scattering and pair distribution function (PDF) analysis. The thermal behaviour of $TITcO_4$ is analysed, and in-depth modelling of its long-range average and short-range local structure is presented. These results are then compared to $TIReO_4$ and other $6s^2$ -containing ABO_4 materials to determine the origin of the differences between these materials.

Experimental Methods

*** Caution! *** 99 Tc is a β emitter ($E_{max.} = 0.29$ MeV). All operations relating to the synthesis of $TlTcO_4$ were performed in a licensed radiochemical laboratory at the University of Las Vegas, Nevada. Appropriate shielding was employed during all manipulations and while loading the sample into a vanadium container for examination.

*** Caution! *** Thallium salts are potentially fatal if swallowed. Appropriate personal protective equipment and safe work procedures were employed during sample preparation and sample manipulation.

Thallium pertechnetate was prepared by cation metathesis from $KTcO_4$ and TlF in deionised water. A thallium(I) fluoride (1.223 g, 5.48 mmol) solution was added dropwise to a solution of $KTcO_4$ (1.095 g, 5.42 mmol) and $TlTcO_4$ precipitated immediately. The mixture was mechanically stirred at room temperature for 1 hour. The solid was allowed to settle, the supernatant was discarded, and the resulting white solid was washed with cold deionised water (3 × 5 mL), isopropanol (3 × 5 mL), and diethyl ether (3 × 5 mL) before being dried at 120 °C for 12 hours. After cooling, $TlTcO_4$ was removed from the vial, weighed (1.477 g, 4.02 mmol, yield 74.2%) and finally sealed in a 6 mm vanadium can and shipped to Oak Ridge National Laboratory (ORNL) for neutron scattering measurements.

Neutron scattering data suitable for neutron PDF (NPDF) analysis were collected with a centre wavelength of 0.8 Å using the POWGEN diffractometer at the Spallation Neutron Source (SNS) located at ORNL.⁴⁹ The data were corrected for instrument background, the incident neutron spectrum, absorption, and multiple scattering events before normalisation. The software PDFgetN3 was used to calculate the NPDF with a Q_{max} of 30.0 Å⁻¹. A Savitzky-Golay filter was applied to the S(Q) for Q > 9.0 Å⁻¹ to reduce the noise in the broad regions of the reciprocal space data. Additional details are provided in the electronic supporting information (ESI).

Structural refinements using the Rietveld method were carried out using the program TOPAS 6.⁵⁰ The background of each pattern was estimated using a 12th-order Chebyshev polynomial. The scale factor, lattice parameters, atomic positions, and atomic displacement parameters (ADPs) were refined simultaneously with the peak profile parameters. Partial NPDFs were calculated using RMCProfile,⁵¹ and the crystal structures were drawn using VESTA.⁵²

The theoretical calculations for TlTcO₄ were performed using the projector augmented wave (PAW) method,⁵³ as implemented in the Vienna Ab initio Simulation Package (VASP) version 5.4.4.⁵⁴ The Perdew-Burke-Ernzerhof (PBE) functional revised for solids (PBEsol) and the Armiento-Mattsson 2005 (AM05) exchange-correlation functionals were employed to study the ground state

structure and electronic interactions.⁵⁵⁻⁵⁷ The basis sets considered for each atom were as follows: TI: $6s^26p^1$, Tc: $4d^55s^2$, O: $2s^22p^4$. The plane-wave cutoff energy was set to 700 eV. A k-point mesh of 11 × 11 × 7 was used in the irreducible Brillouin zone, utilising Monkhorst Pack (MP) grids.⁵⁸ The force minimisation and convergence criteria were set to 10^{-9} eV for electronic convergence and 10^{-3} eV for ionic relaxation, respectively. To compute the electronic structure of TITcO₄, the Tran-Blaha modified Becke-Johnson (TB-mBJ) potential was employed in conjunction with the traditional generalised gradient approximation (GGA) method incorporated in VASP.⁵⁹⁻⁶² The TB-mBJ potential is known to effectively address the band gap of materials, particularly for insulators and semiconductors. The impact of spin-orbit coupling (SOC) was also considered. Our results indicate that the inclusion of SOC has almost no impact on the partial density of states (PDOS) for the atoms. Isosurface maps illustrating bonding interactions through the electron localisation function (ELF) were generated for the structures of TITcO₄ determined from the NPDF fits at 50 K. The visualisation of the ELF was subsequently performed using VESTA.⁵²

Results and Discussion

(i) Neutron Powder Diffraction and Rietveld Analysis

Neutron powder diffraction (NPD) data were collected at 50, 300, 450, and 600 K (Table S1). These temperatures were chosen based on the orthorhombic-to-tetragonal phase transition observed in the previous SXRD study.³³ The 50 K data were measured to minimise thermal motion, thus allowing deconvolution of static and dynamic disorder. Although the fit to the 50 K data is not optimal, possibly due to disorder, the important structural features are evident. The orthorhombic *Pnma* pseudo-scheelite structure consists of a network of TlO₁₀ polyhedra and TcO₄ tetrahedra. Considering that the eight shortest Tl–O bond distances vary between 2.689(14)–3.052(6) Å, it appears that Tl⁺ is displaced towards the corner of an ideal cube by the Tl⁺ 6s² lone pair electrons directed to the adjacent cube edge, resulting in two long Tl–O distances. There are two longer Tl–O contacts that become important in the high-temperature tetragonal structure (see below). Considering these, the bond distortion index of the resulting TlO₁₂ polyhedra is 0.08205. Although the TcO₄ tetrahedra are distorted, there is a narrow range of Tc–O bond lengths between 1.724(10)–1.767(16) Å with an average of 1.745(14) Å. The O–Tc–O bond angles in the tetrahedra range from 105.6(8)–111.9(5) °. The same orthorhombic *Pnma* model was also used to fit the data obtained at 300 and 450 K (Figure S2).

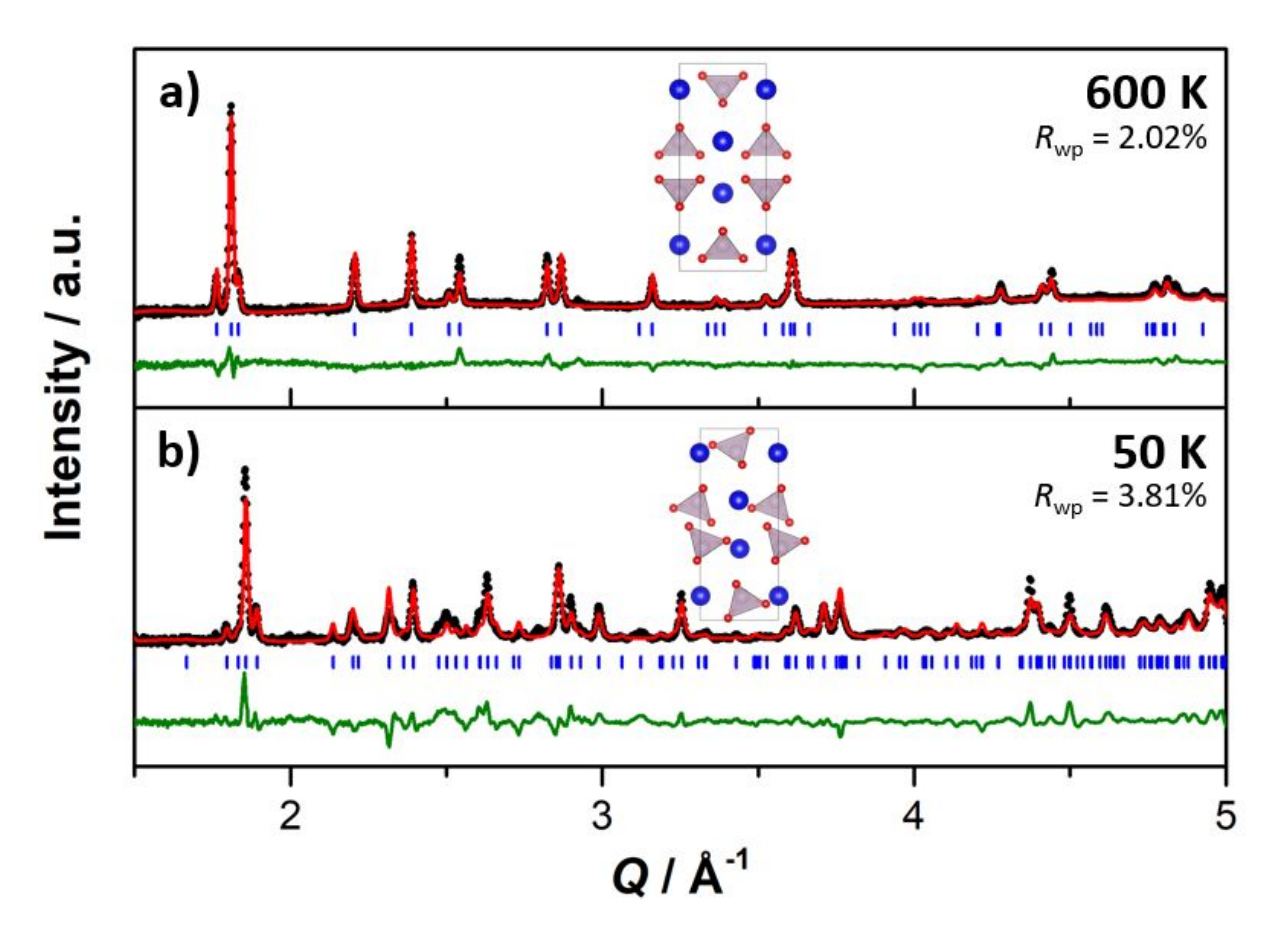


Figure 2: Rietveld refinements to the neutron Bragg data of TlTcO₄, collected on the POWGEN diffractometer at (a) 600 K refined to the tetragonal *I*4₁/*amd* space group, and (b) 50 K refined to the orthorhombic *Pnma* space group. The black circles represent the data, the red line represents the fit to the data, the green line represents the difference between the data and the fit, and the blue dashes represent the space group-allowed reflections.

A previous SXRD study concluded that TITcO₄ underwent a phase transition from orthorhombic *Pnma* to tetragonal $I4_1/amd$ at ~500 K.³³ This was based on a lack of evidence of the (114) reflection, which is allowed in $I4_1/a$ but forbidden in $I4_1/amd$ by the 2h + l = 4n reflection condition. The orthorhombic *Pnma* to tetragonal $I4_1/amd$ phase transition is allowed to be continuous (by condensation of the M_4^+ mode, see Figure S1). However, other orthorhombic *Pnma* pseudoscheelite structures (such as CsBO₄, B^{7+} = Tc, Ru, Re, Os; and RbRuO₄) display a first-order phase transition from orthorhombic *Pnma* to tetragonal $I4_1/a$.^{32, 33, 36, 63} These two tetragonal structures differ by the rotation of the BO_4 tetrahedra that is allowed in $I4_1/a$ but not in $I4_1/amd$. Attempts to fit both models to the high temperature 600 K dataset returned similar qualities of fit (R_{wp} = 2.00% for $I4_1/a$ vs. 2.02% for $I4_1/amd$; see Figure S3). Therefore, the tetragonal $I4_1/amd$ model was adopted at 600 K in line with the suggestion of Kennedy *et al.*³³ The quality of the fit to the 600 K dataset. The Tl⁺ cation is

12-coordinate in the tetragonal $I4_1/amd$ structure with four Tl–O bonds at 2.942(7) and a further eight at 3.352(4). The bond distortion index of the TlO₁₂ polyhedra is noticeably smaller than seen at 50 K (0.0567 vs. 0.08205).

The temperature dependence of the unit cell parameters and Tc-O distances is displayed in Figure 3: Due to the sparsity of data points in the current NPD study, values from the previous SXRD study are also presented,³³ and these are in good agreement with the current study. The lattice parameters display conventional thermal expansion, with the a and b lattice parameters becoming equal above 500 K, corresponding to the orthorhombic-to-tetragonal phase transition. The temperature dependence of the ADPs shows the values for the Tc^{7+} and O^{2-} atoms increasing between 50 and 300 K before dropping at 450 K (Figure S4). This is thought to be a result of the rare isosymmetric orthorhombic Pnma to orthorhombic Pnma phase transition at ~400 K.³³

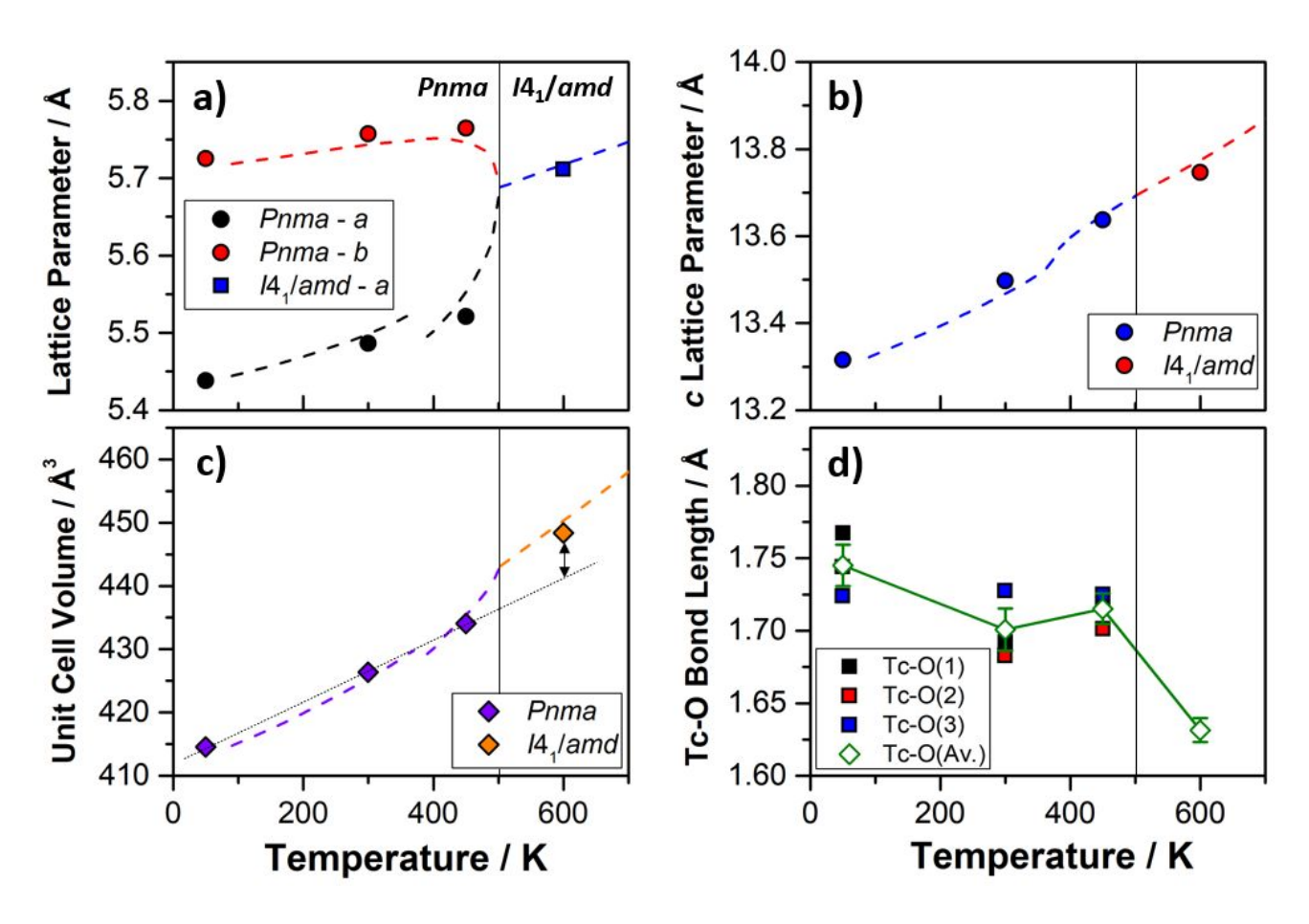


Figure 3: Temperature dependence of the (a,b) lattice parameters, (c) unit cell volume, and (d) the Tc–O bond distances for TlTcO₄ derived from the Rietveld refinements of the neutron powder diffraction data. Where not shown, the error bars are smaller than the symbols. The dashed lines in (a–c) are the results from the previous synchrotron X-ray diffraction study.³³ The dotted line in (c) drawn to guide the eyes.

As evident from Figure 3, the unit cell volume of the tetragonal $I4_1/amd$ phase is significantly larger than that of the extrapolated orthorhombic Pnma phase. Although only one temperature point is taken above the phase transition in the current NPD study, the previous SXRD refinements show the same trend.³³ Similar behaviour was recently described in TlReO₄, and Saura-Múzquiz *et al.* proposed that ordering of the Tl⁺ $6s^2$ lone pairs in the lower symmetry phase caused a more efficient packing of the structure.⁴⁸ By analogy, we postulate that the $6s^2$ lone pairs in TlTcO₄ are ordered in the orthorhombic phase and disordered in the tetragonal phase (Figure S5). This hypothesis is supported through a comparison of the monoclinic I2/b and tetragonal $I4_1/a$ structures of NdNbO₄ (Nd³⁺: $6s^0$) and BiVO₄ (Bi³⁺: $6s^2$).^{24, 64, 65} The tetragonal $I4_1/a$ unit cell volume in NdNbO₄ is smaller than the unit cell volume extrapolated from the monoclinic I2/b phase. In contrast, it is larger in BiVO₄ due to the disordering of the $6s^2$ lone pairs (Figure S6).

An additional advantage of NPD is that neutrons are scattered isotropically due to the short range of their interaction. This makes them more sensitive to the small displacements of atoms from their equilibrium positions, leading to greater precision in the refined ADPs compared to SXRD studies. Although oxygen is a relatively weak X-ray scatterer (Z = 8) compared to Tl⁺ (Z = 81) and Tc⁷⁺ (Z = 43), the coherent neutron scattering length of the three atoms are comparable ($b_0 = 5.8$, $b_{Tc} = 6.8$ fm, $b_{Tl} = 8.8$), leading to greater sensitivity to the Tc–O bond distances. As observed in Figure 3: , the Tc–O bond lengths decrease upon heating. This has been observed in several other ABO_4 structures, including CaMoO₄ and CsReO₄, 36, 67 and has been correlated with the onset of rotational disorder in the rigid BO_4 tetrahedra units. It is possible that the orthorhombic-to-tetragonal phase transition in TlTcO₄ may be related to the onset of rotational disorder in the rigid TcO₄ units. However, observation of the short-range local structure is required to verify this possibility.

(ii) Neutron Total Scattering and Pair Distribution Function Analysis

NPDF data of TITcO₄ at 50, 300, 450, and 600 K are plotted in Figure 4. The first narrow peak at ~1.72 Å corresponds to the first Tc–O pair within the TcO₄ tetrahedra and shows neither splitting nor broadening at any of the measured temperatures. The first O–O distance, corresponding to the edge of the TcO₄ tetrahedra, results in a consistent peak at ~2.80 Å. Rietveld analysis of the NPD Bragg data shows the Tc–O bond lengths decrease upon heating, from an average of 1.731(14) Å at 50 K to 1.630(9) Å (a ~6% decrease) at 600 K. However in the NPDF, the Tc–O bond length at ~1.72 Å remains unchanged across all measured temperatures, suggesting the Tc–O bond length shortening observed in the NPD Bragg data is unphysical. That neither the first Tc–O nor O–O distances change significantly over the measured temperature range implies the presence of rigid TcO₄ tetrahedra, consistent with other PDF studies of ABO_4 scheelite-type oxides.^{34, 36, 48, 67, 68}

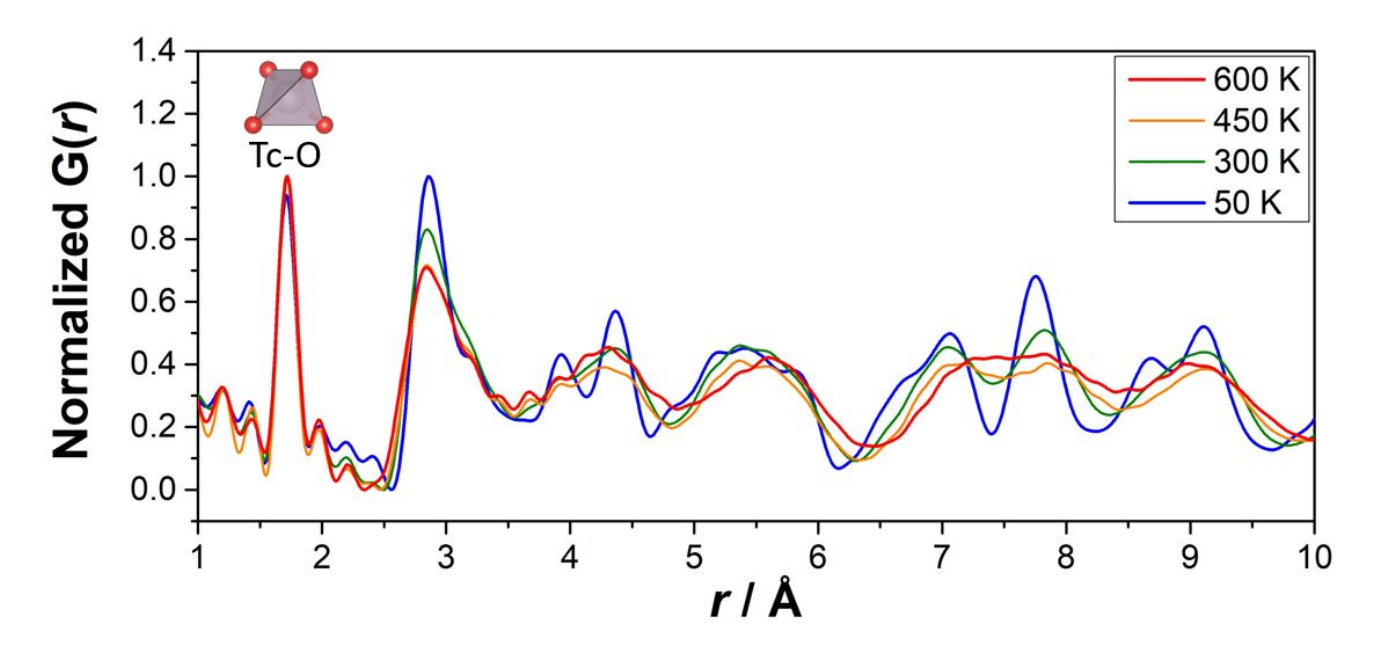


Figure 4: Variable temperature neutron pair distribution function data of TlTcO₄ at 50 (blue), 300 (green), 450 (orange), and 600 K (red).

Stereochemically active ns^2 lone pairs often cause cations to disorder through well-defined displacements from their centrosymmetric positions (giving a static contribution to the ADPs) as well as increased thermal motion (giving a dynamic contribution).⁶⁹⁻⁷¹ Data were measured at 50 K to minimise the thermal disorder, resulting in sharper peaks at high r. Fits were conducted using the long-range average orthorhombic Pnma model over a range of 1.0–30 Å (Figure 5). This model returned a poor fit especially at low r, with a large residual observed across the entire fitting range. The failure to accurately fit the high r region to the orthorhombic model suggests a subtle symmetry lowering. The

feature at ~2.84 Å was particularly poorly fitted, with partial PDFs revealing this region corresponds to the Tl–O distances within the TlO₁₀ polyhedra and the O–O distances across the TlO₁₀ polyhedra and TcO₄ tetrahedra (Figure S7). Fits were attempted with both rigid (single Tc–O distance and O–Tc–O angles constrained to be 109.5 °) and flexible TcO₄ tetrahedra. However, neither approach was able to reproduce the sharp feature at ~2.84 Å. Fits were also performed to the higher symmetry tetragonal $I4_1/a$ and $I4_1/amd$ scheelite-type structures, which also returned poor fits (Figure S8).

Fits were then undertaken using the monoclinic $P2_1/c$ structural model seen in other $6s^2$ -containing ABO_4 materials, such as the long-range average and short-range local structure of TlReO₄ at room temperature and the short-range local structure of PbWO₄.^{48, 72} This monoclinic model involves more complex distortion of the TlO₁₀ polyhedra associated with short-range disorder of the Tl⁺ $6s^2$ lone pair electrons and provides the best fit to the data over a range of 1.0–30 Å, as shown in Figure 5. This implies that the local structures of TlTcO₄ and TlReO₄ are the same despite their different long-range average structures. A key feature of the monoclinic $P2_1/c$ TlReO₄ structure is the displacement of the Tl⁺ cations from the centre of the Tl⁺ polyhedra, resulting in more significant variability in the Tl–O bond lengths and rotation of the ReO₄ tetrahedra. Evidently, similar displacements occur in TlTcO₄, with the same features observed in the 100 K dataset taken on the NOMAD diffractometer (Figures S9–10), as well as the 300 and 450 K NPDF datasets (Figures S11–13). As detailed below, density functional theory (DFT) calculations show the ground state energy of the monoclinic $P2_1/c$ structure to be lower than that of the orthorhombic Pnma structure (Tables S2–3).

Fits were also performed across different distance 'windows', with better fits were achieved by using 10 Å windows across the data (Figure S14). This also resulted in a more distorted structure at low *r* and differences in the TcO₄ volume. This suggests nanodomains may form at lower temperatures related to the 'freezing in' of Tl⁺ 6s² lone pair disorder and the isosymmetric orthorhombic *Pnma* to orthorhombic *Pnma* phase transition that are difficult to model, also potentially explaining the suboptimal fitting to the NPD at 50 K. In fitting the NPDF in 10 Å windows, the less-local fits provide an 'averaging' of these more-local features to better fit the data. Further confirmation using additional techniques, such as transmission electron microscopy or solid-state nuclear magnetic resonance spectroscopy, would be required to better model these contributions.

There is an apparent disconnect between the long-range average and short-range local structures of TlTcO₄. At 50 K, the long-range NPD Bragg data were best fit using the orthorhombic *Pnma* model consisting of TlO₁₀ polyhedra with several different Tl–O bond lengths and distorted

TcO₄ tetrahedra. The short-range NPDF data revealed that the TcO₄ tetrahedra are rigid and a greater distribution of Tl–O bond distances within the Tl⁺ polyhedra (Figure S17), where the long and flexible Tl-O bonds allow for the rigid TcO₄ tetrahedra to rotate freely. This degree of rotational freedom in the ABO₄ scheelite-derived structures is due to the A-O-B connectivity that acts as a 'hinge'.⁶⁷ Unlike in perovskite-derived structures where the BX_6 octahedra are corner sharing, the TcO_4 tetrahedra are not directly connected, relaxing the requirement of coherent tetrahedra rotations. It is this lack of connectivity that leads to incoherent TcO4 tetrahedra rotations and translations that Rietveld refinements may model as a combination of increased ADPs and Tc-O bond shortening, as also seen in RbReO₄ and CsReO₄. ^{34, 36} Furthermore, the monoclinic P2₁/c structural model can be derived from the tetragonal $I4_1/amd$ aristotype by rotation of the TcO₄ tetrahedra about the a-axis (similar to those observed in the orthorhombic *Pnma* structure) governed by a M₄⁺ mode, and about the *b*-axis (analogous to that observed in the tetragonal $I4_1/a$ structure) governed by a Γ_3^+ mode (Figure S1). It is postulated that locally both the M_4^+ and Γ_3^+ modes are present, and the lack of direct connectivity reduces the correlation of the rotations. This explains why the long-range average structure is best fitted to the orthorhombic $\textit{Pnma}\ (M_4^+)$ structure, as the TcO_4 tetrahedra rotations governed by the Γ_3^+ mode are uncorrelated and separated by ~18 Å.

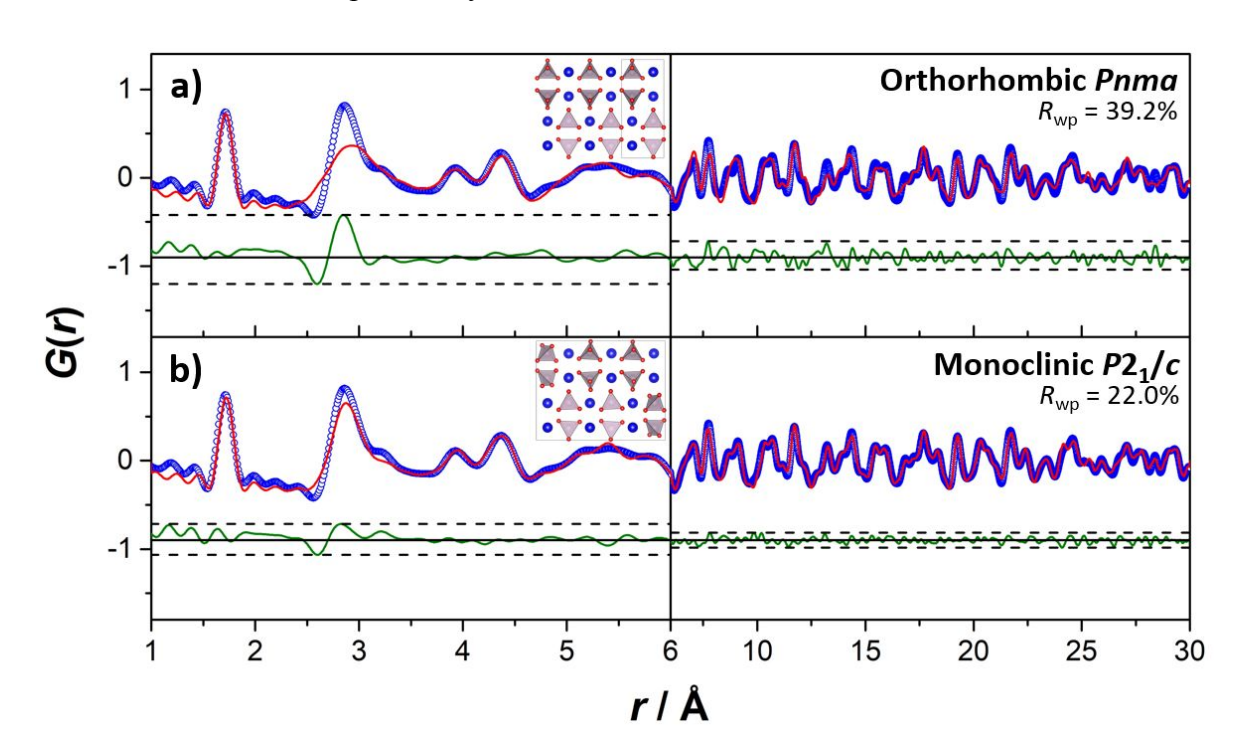


Figure 5: Neutron pair distribution function data collected at 50 K on the POWGEN instrument. Fits to the data were conducted with (a) the long-range orthorhombic Pnma model, and (b) the long-range monoclinic $P2_1/c$ model observed in TIReO₄. The blue circles represent the data, the red line represents the fit to the data, and the green line represents the difference between the two. The dashed lines indicate the maximum and minimum in the difference curve across the plotted r ranges.

The fitting process was repeated for the 600 K dataset (Figure S15), recalling that 600 K is above the orthorhombic-to-tetragonal phase transition.³³ All four models (orthorhombic *Pnma*, tetragonal $I4_1/a$ and $I4_1/amd$, and monoclinic $P2_1/c$) returned a similar goodness of fit, most likely due to the greater amount of thermal motion and broader NPDF peaks at higher temperatures. Despite these broadened features, the Tc–O peak at ~1.72 Å remains relatively unchanged between the 50 and 600 K datasets, while the prominent peak at ~2.84 Å shows significantly less thermal broadening compared to the other peaks within the NPDF datasets reflecting the rigid TcO₄ tetrahedra (Figure 4). Although the local features at ~2.84 Å are best fit using the monoclinic $P2_1/c$ model, the less local (10–30 Å) range is fit equally well between the four models (Figure S16). This suggests that the Tl⁺ 6 s^2 lone pairs are still sterically active at high temperatures, but with a short (>10 Å) correlation length.

(iii) Ground State Energy Calculations Using Density Functional Theory

Tables S2-3 report the ground state energies for the four possible structures of TITcO₄ from DFT calculations: tetragonal $I4_1/a$, tetragonal $I4_1/amd$, orthorhombic Pnma, and monoclinic $P2_1/c$ calculated using the PBE, PBEsol, and AM05 functionals. For each structure, the calculations converged to a physically reasonable model and the calculated unit cell parameters are in acceptable agreement with the experimentally observed values.³³ Irrespective of the functional employed, the tetragonal $I4_1/a$ structure has the lowest energy and the tetragonal $I4_1/amd$ the highest, with the ground state energy of the monoclinic $P2_1/c$ structure invariably lower than that of the orthorhombic Pnma structure (Table S3). That these functionals all predicted the tetragonal $I4_1/a$ structure to be the ground state, in contrast to the experimental findings, reflects the challenges of investigating the structure and physical properties of materials with highly polarizable ions. The failure of these functionals to correctly predict the experimentally observed ground state mirrors the situation in BiVO₄.⁷³ Liu *et al.* reported that the relative energies of the experimentally observed tetragonal $I4_1/a$ and monoclinic I2/b structures could only be reproduced using complex hybrid functionals as a consequence of the need to accurately describe the Bi³⁺ 6s² lone pair electrons by including the polarizability of the Bi³⁺ cation.⁷³ These authors did not consider the possibility of local scale distortions.

Figure 6 illustrates the band structure and PDOS for TlTcO₄ in the monoclinic $P2_1/c$ structure. Essentially identical results were obtained for calculations assuming the orthorhombic Pnma structure (Figures S18). This shows that TlTcO₄ is a direct band gap semiconductor with a band gap of 2.53 eV, as estimated using the TB-mBJ potential. The valence band is predominantly compromised of the O p and Tl s states, while the conduction band is mainly derived from Tc d states. The Tl 6s states are

present at the top of the valence band and show significant hybridisation with the O 2p states, with minimal involvement from the Tc states. This is a characteristic of stereochemical active $6s^2$ electrons. This is demonstrated through ELF calculations, illustrated for the <001> plane in Figure 7, that indicate localisation of the Tl 6s states and presumed stereochemical activity. Conversely, the O 2p states exhibit moderate localisation, while the Tc states show very little.

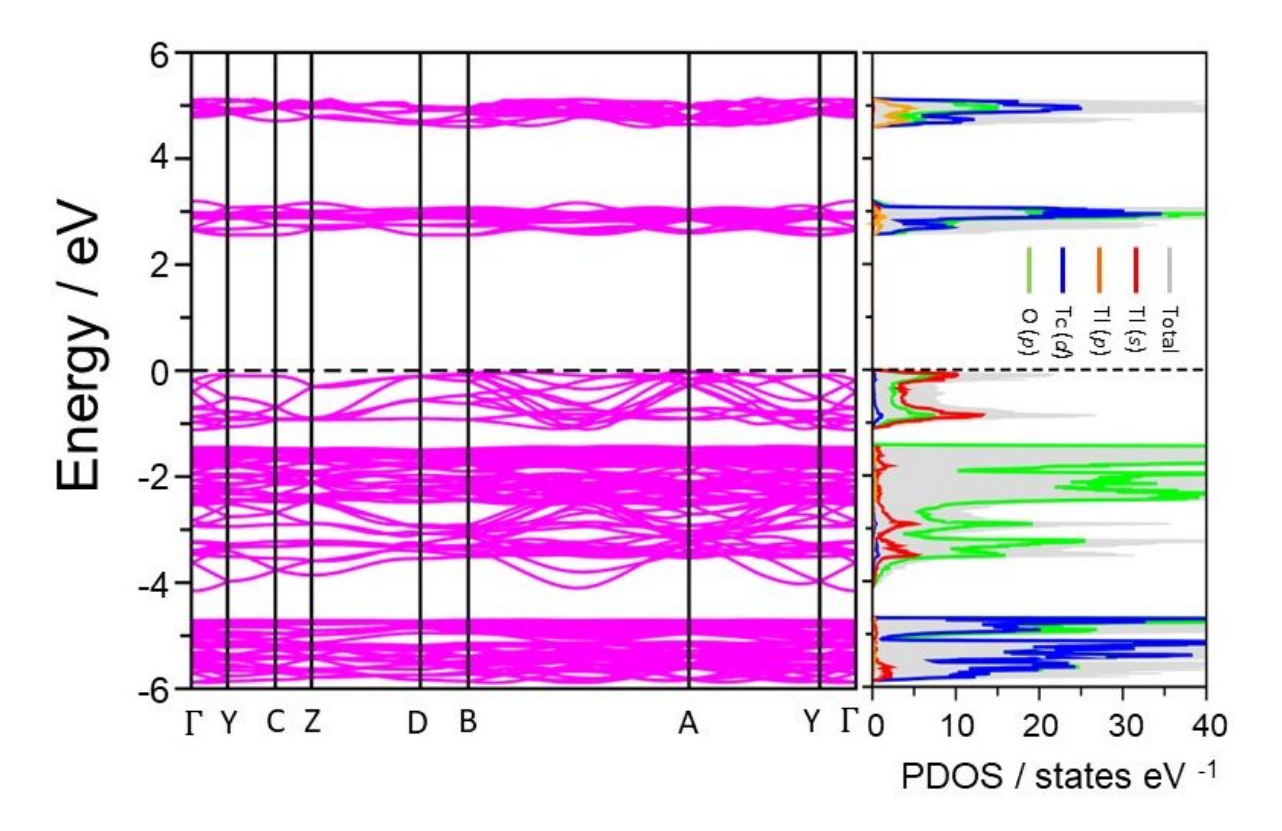


Figure 6: Electronic band structure and partial density of states (PDOS) of TITcO₄ in the monoclinic $P2_1/c$ structure calculated using the Tran-Blaha modified Becke-Johnson (TB-mBJ) potential, showing a bandgap of 2.53 eV.

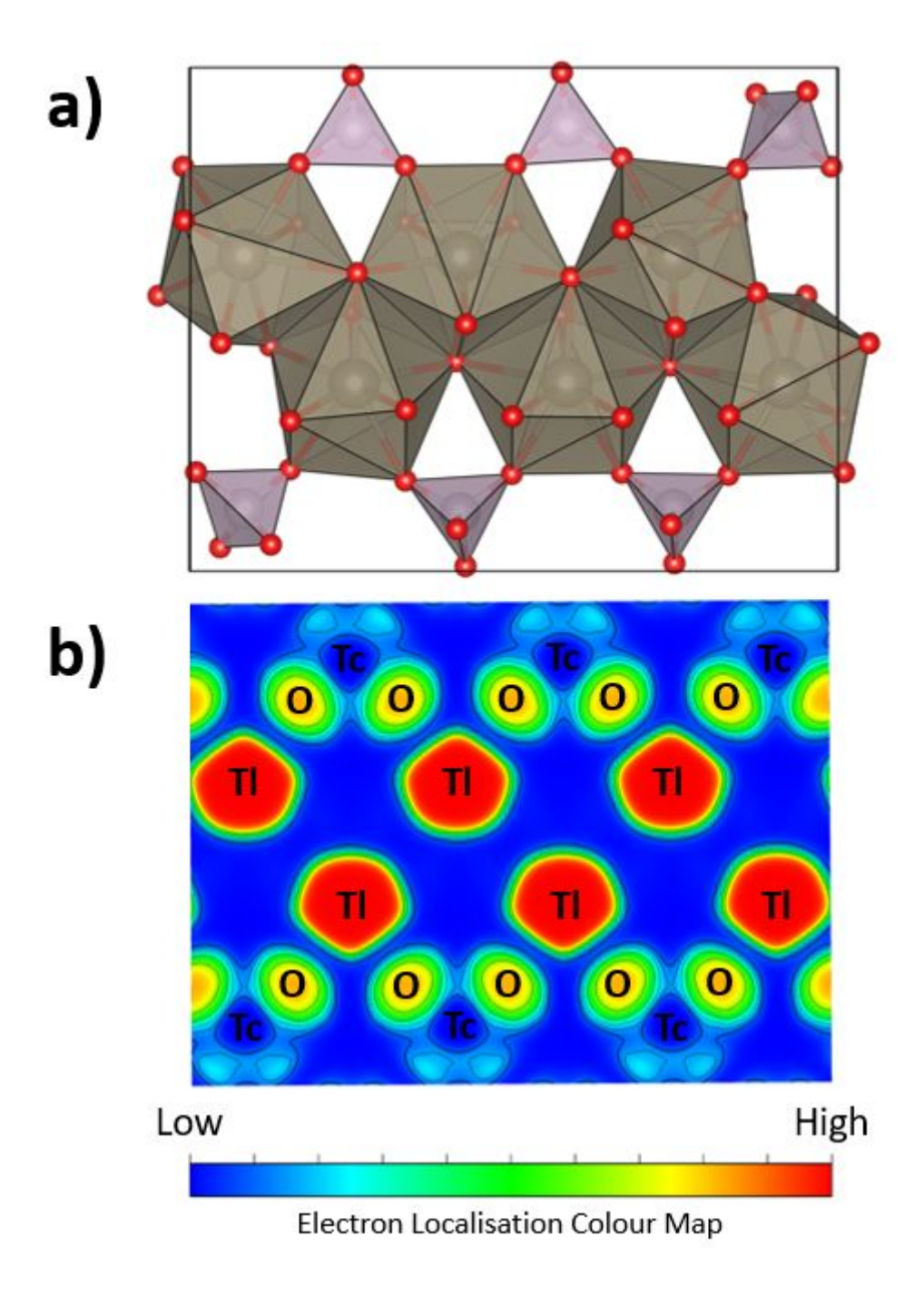


Figure 7: (a) Structural model of TITcO₄ in the monoclinic $P2_1/c$ space group, fit from the 50 K POWGEN neutron pair distribution function data. (b) Isosurface maps illustrating bonding interactions through the electron localisation function (ELF) in the <001> plane generated for the geometry-optimised structure of TITcO₄ in the monoclinic $P2_1/c$ space group.

(iv) <u>Comparison Between ABO₄ Structures with 6s² Lone Pair Electrons</u>

TITcO₄ can now be placed in the context of other ABO_4 structures with $6s^2$ lone pair electrons. At 300 K, TITcO₄ (orthorhombic Pnma),³³ TIReO₄ (monoclinic $P2_1/c$),³² PbWO₄ (tetragonal $I4_1/a$),⁷² and BiVO₄ (monoclinic I2/b)⁷⁶ each display different long-range average structures. The impact of the stereochemically active A-site $6s^2$ electron lone pairs on the local structure appears to be dependent on a combination of the size, oxidation state, and polarizability of the A- and B-site cations. These are shown in Figure 8 and Table 1, and are discussed below.

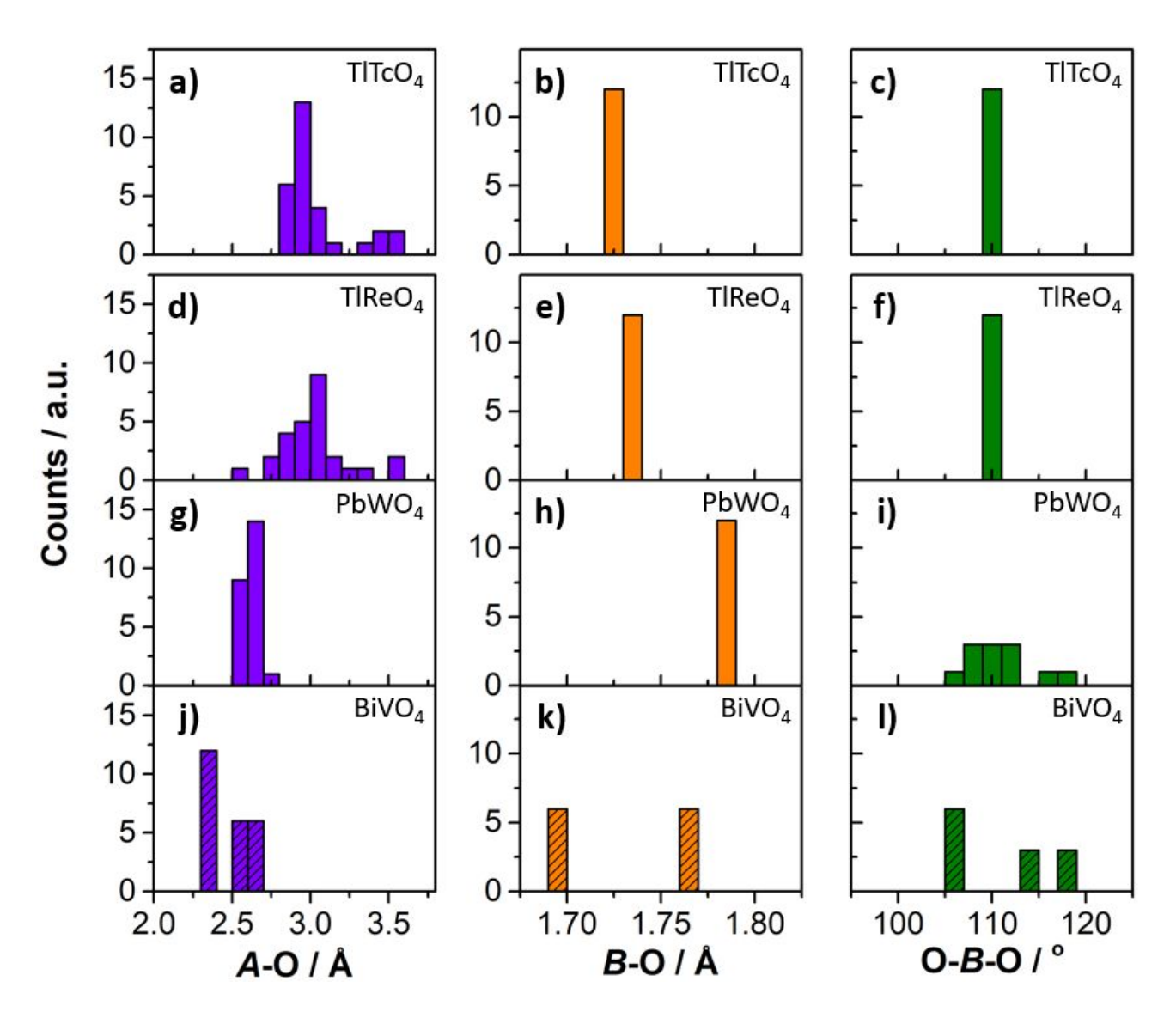


Figure 7: The A–O, B–O bond lengths, and O–B–O bond angles from (a–c) TlTcO₄ from this work, (d–f) TlReO₄ taken from Saura-Múzquiz *et al.*, ⁴⁸ (g–i) PbWO₄ taken from Mullens *et al.*, ⁷² and (j–l) BiVO₄ taken from Sleight *et al.* ⁷⁶ All data is taken from the neutron pair distribution function fits at 300 K to the monoclinic $P2_1/c$ model, except for BiVO₄ (crossed histogram bars), which is the long-range average structure in the monoclinic I2/b space group.

Table 1: Calculated AO_8 polyhedra and BO_4 tetrahedra volumes for various ABO_4 materials containing $6s^2$ lone pair-containing A-site cations. For the monoclinic $P2_1/c$ space group, the volumes are averaged over the three different A- and B-sites.

	Space Group	AO ₈ Volume (Å ³)	BO ₄ Volume (Å ³)	Reference
TITcO ₄	$P2_1/c$	52.1	2.62	This work.
TIReO ₄	$P2_1/c$	55.0	2.67	48
PbWO ₄	$P2_1/c$	32.2	2.91	72
BiVO ₄	<i>I</i> 2/ <i>b</i>	26.6	2.63	76

The A–O–B connectivity makes it reasonable to assume that distortions of the AO_8 polyhedra and BO_4 tetrahedra are related. Across the 5p block elements (A = Tl $^+$, Pb $^{2+}$, Bi $^{3+}$), the oxidation state increases resulting in shorter A–O bonds and smaller AO_8 polyhedra (Table 1). As seen in Figure 8, the larger oxidation state A-site cations result in less flexible AO_8 polyhedra and a smaller distribution of the A–O bond lengths. As the AO_8 polyhedra get smaller, the flexibility of the BO_4 tetrahedra becomes more important. While the TcO $_4$ and ReO $_4$ tetrahedra remain rigid, the WO $_4$ tetrahedra distort through relaxation of the O–W–O bond angles and the VO $_4$ tetrahedra distort through variations in both the O–V–O bond angles and the V–O bond lengths. Likewise, the choice of nd^0 element on the B-site affects the degree of polarizability, with the VO $_4$ tetrahedra in BiVO $_4$ (V: $3d^0$) exhibiting a greater amount of distortion than the TcO $_4$ tetrahedra in TlTcO $_4$ (Tc: $4d^0$) and the ReO $_4$ tetrahedra in TlReO $_4$ (Re: $5d^0$).

The PDOS for TlTcO₄ is very similar to that of TlReO₄ and PbWO₄ (Figures S19), despite these materials having different long-range average structures at 300 K.^{48, 72} The PDOS is, however, significantly different from that reported for BiVO₄ where the Bi 6s states are significantly further below the Fermi level (~9 eV vs. 1 eV for TlTcO₄).⁷³ Presumably strong hybridisation of the 6s states of Pb and Tl with O p or metal d states pushes these levels closer to the conduction band edge, whereas the higher oxidation state of Bi reduces the hybridisation of the Bi 6s states with the oxygen states. Indeed, near the Fermi level BiVO₄ features only O p states in the valence bands. The implication is that the 6s electrons do not participate significantly in bonding, rather they remain as lone pairs and exhibit an obvious stereochemical influence. It can be speculated that this difference in the PDOS may be correlated with the photocatalytic properties of these oxides.

The question remains as to why TITcO₄ and TIReO₄ have the same monoclinic $P2_1/c$ local structure but different long-range average structures. Previous studies have shown that all other ATcO₄ and AReO₄ salts (A^+ = Na, K, Rb, Ag, Cs) are isostructural.^{30, 32, 33} Bastide's analysis of the r_A/r_O and r_B/r_O ratios in the ABO₄ materials suggests that TIReO₄ should adopt a tetragonal $I4_1/a$ structure similar to RbReO₄,³⁵ as the two A-site cations are approximately the same size (TI⁺ = 1.59 vs. Rb⁺ = 1.61 Å).¹⁷ TIReO₄ exhibits the tetragonal $I4_1/a$ structure at low (<150 K) and high temperatures (>400 K), with the room temperature monoclinic $P2_1/c$ structure the result of long-range ordering of the TI⁺ 6 s^2 lone pairs.⁴⁸ Since Tc⁷⁺ is slightly smaller than Re⁷⁺ (0.37 vs. 0.38 Å),¹⁷ as evident from the sharp B-O peaks at 1.72 and 1.74 Å in the NPDF data of TITcO₄ and TIReO₄ respectively, it is possible that this small change in the B-site cation ionic radii is sufficient to favour the formation of the long-range orthorhombic Pnma, rather than the tetragonal $I4_1/a$ structure ($r_{Tc}/r_O \sim 0.27$ vs. $r_{Re}/r_O \sim 0.28$).

The long-range average monoclinic $P2_1/c$ structure of TlReO₄ at room temperature is derived from the tetragonal $I4_1/amd$ aristotype by rotations of the ReO₄ tetrahedra associated with the *irreps* Γ_3^+ and M_4^+ .³² In this structure, TlReO₄ has two distinct ReO₄ tetrahedra sites rotated about the *b*-axis (associated with the *irrep* Γ_3^+ , analogous to the tetragonal $I4_1/a$ to tetragonal $I4_1/amd$ phase transition), and one distinct ReO₄ tetrahedra site rotated about the *a*-axis (associated with the *irrep* M_4^+ , analogous to the orthorhombic *Pnma* to tetragonal $I4_1/amd$ phase transition). Although the same *irreps* are present in the local structure of TlTcO₄, the opposite trend is observed. There are two distinct TcO₄ tetrahedra sites rotated about the *a*-axis, and one rotated about the *b*-axis (Figure S18). Evidently, the 'averaging' of these leads to the observation of different long-range average structures.

A further difference between TITcO₄ and TIReO₄ is the lack of a re-entrant phase transition observed in TITcO₄. Phase transitions can be driven by the ability of the $6s^2$ lone pairs to macroscopically align, leading to a lowering of symmetry and a decrease in unit cell volume due to the more compact structure. This is seen in TIReO₄ where the room temperature structure is monoclinic $P2_1/c$ due to the ability of the $6s^2$ to align macroscopically, before an increase in temperature leads to greater thermal motion and a breakdown of this long-range ordering. ⁴⁸ No such macroscopic ordering is observed in TITcO₄ due to the larger thermal motion of the TcO₄ tetrahedra compared to ReO₄ (Figure S19). This was similarly seen in work by Amarasinghe *et al.*, where greater rotational disorder was observed in the lighter MoO₄ tetrahedra of NaRE(BO₄)₂ (RE³⁺ = Ln, Y; B⁶⁺ = Mo, W) compared to the heavier WO₄ tetrahedra (95 vs. 184 amu). ²⁵ As Tc⁷⁺ is almost half of the atomic mass of Re⁷⁺ (98 vs. 186 amu), a similar sensitivity to temperature and larger thermal displacements is expected. The greater susceptibility of the TcO₄ tetrahedra to rotate may also explain the differences in the

thermal expansion behaviour of the two ammonium salts NH_4TcO_4 and NH_4ReO_4 at different temperatures.²³

Conclusions

A detailed variable temperature neutron total scattering study – combining both NPD and NPDF – to understand the long-range average and short-range local structure of TlTcO₄ was conducted. In the long-range average structure, an orthorhombic Pnma to tetragonal $I4_1/amd$ phase transition occurred before 600 K, consistent with previous SXRD studies.³³ This is the first observation of such a phase transition, with other orthorhombic Pnma pseudo-scheelite structures undergoing a first order phase transition to the tetragonal $I4_1/a$ scheelite-type structure.^{32, 33, 36, 63} Modelling the short-range local structure required a lower symmetry monoclinic $P2_1/c$ model due to the stereochemistry of the Tl⁺ $6s^2$ lone pairs. This is facilitated by the flexible Tl⁺ polyhedra and rigid TcO₄ tetrahedra. The stereochemistry of the Tl⁺ $6s^2$ lone pair persisted above the long-range orthorhombic Pnma to tetragonal $I4_1/amd$ phase transition, albeit on the local scale.

Several anomalies were observed in the Rietveld refinements to the NPD data, such as large ADPs at low temperature and a shortening of the Tc–O bond distance upon heating. Using NPDF, these structural anomalies were resolved by devising a model with longer, more flexible Tl–O bonds that allow for the rotation of rigid TcO₄ tetrahedra units. This model was then supported by DFT calculations. Considering both the long-range average and short-range local structures of TlTcO₄, a more holistic structural model was developed. At low temperatures, the stereochemical activity of the Tl⁺ $6s^2$ lone pairs is 'frozen' into the structure, resulting in static rotations of the TcO₄ tetrahedra. As the material is heated, the TcO₄ tetrahedra begin to rotate as governed by the Γ_3^+ and M_4^+ modes. The Γ_3^+ rotations appear to be less correlated than the M_4^+ modes, resulting in the observation of the orthorhombic *Pnma* structure in the long range. At ~500 K, the thermal motion is large enough such that the rotations shift from coherent to incoherent, resulting in an 'averaging out' of the rotations and the observation of the higher symmetry tetragonal $I4_1/amd$ structure. However, the $6s^2$ lone pairs remain stereochemically active on the local scale, as observed in the NPDF fits. The orthorhombic *Pnma* to tetragonal $I4_1/amd$ phase transition is seemingly the result of a change in the correlation length of the Tl⁺ $6s^2$ lone pairs, leading to a larger unit cell volume due to their uncorrelated displacements.

This study of TlTcO₄ was put into the larger context of other ABO_4 structures containing $6s^2$ lone pairs, including TlReO₄, PbWO₄, and BiVO₄. Each of these oxides has a different long-range average structure at 300 K. However, common trends in the local scale distortions necessary to

accommodate the stereochemically active $6s^2$ lone pair were identified. Although TITcO₄ and TIReO₄ disorder in a similar way, a combination of the size of the *A*-site polyhedra and the choice of nd^0 *B*-site cation leads to different disordering phenomena. These include large ranges of *A*-O bonds, flexibility in the O-*B*-O tetrahedra bond angles, and distortion of the *B*-O bond lengths. This gives a rich tapestry of mechanisms that can be further implemented when fine-tuning the local scale interactions of atoms for the next generation of functional energy materials. The role of polarizability of the *B*-site cations is worthy of further exploration, especially with the large distortions of the VO₄ tetrahedra observed and the lack of NPDF data available for BiVO₄. Unfortunately, no such Bi*B*O₄ analogous structures are currently known, with Bi*B*O₄ [B^{5+} = Nb ($4d^{10}$), Sb ($4d^{10}$), Ta ($5d^{0}$)] crystallising in different structures consisting of BO_6 octahedra.⁷⁷⁻⁷⁹

Optimisation of the structures using the commonly employed PBE, PBEsol, and AM05 exchange-correlation functionals within VASP indicated that the monoclinic $P2_1/c$ structure was more stable than the orthorhombic Pnma model that describes the long-range average structure of TITcO₄ below 500 K. However, for each of these functionals the tetragonal $I4_1/a$ structure was predicted to be the energetic ground state, demonstrating the challenges of accurately describing the $6s^2$ lone pair electrons and polarizability of the Tl⁺ cation. While it may be possible to identify a hybrid functional that correctly predicts the relative energy of these phases, it is evident that there is no unique universal exchange-correlation functional appropriate for these types of oxides, as seen with other ABO_4 metal oxides. 38,73

Finally, this work adds to the suite of studies demonstrating the necessity of considering both the long-range average and short-range local structure of *ABO*₄ scheelite-related materials, which have found application as photocatalysts, selective oxidation catalysts, and potential nuclear waste forms.³³, ^{76, 80} Relationships such as these are of great significance, and additional experimental studies of the local structures, partnered with DFT calculations, are required to identify additional ways of fine-tuning these local disordering features.

Conflicts of Interest

There are no conflicts of interest to declare.

Supporting Information

The Supporting Information is available free of charge at XXXXXX.

Variable temperature Rietveld refinements of TlTcO₄, space group analysis at 600 K, atomic displacement parameters, depiction of structures, partial PDF fits, density functional theory calculations, and variable *r* range NPDF fits.

Acknowledgements

We acknowledge the support of the Australian Research Council for this work that was facilitated by access to Sydney Analytical, a core research facility at the University of Sydney. BGM thanks the Australian Institute for Nuclear Science and Engineering for a PGRA scholarship and the Australian Nuclear Science and Technology Organisation for a United Uranium Scholarship. MSM gratefully acknowledges the financial support from the Comunidad de Madrid, Spain, through an "Atracción de Talento Investigador" fellowship (2020-T2/IND-20581). A portion of this research used resources at the Spallation Neutron Source, a DOE Office of Science User Facility operated by the Oak Ridge National Laboratory [beamtime on NOMAD (IPTS #30368) and POWGEN (IPTS #26502) greatly acknowledged]. At UNLV, this material is based upon work performed under the auspices of the Consortium on Nuclear Security Technologies (CONNECT) supported by the Department of Energy/National Nuclear Security Administration under Award Number(s) DE-NA0003948. Supratik Mukherjee acknowledges DRDO, India, for the financial support provided through ACRHEM (DRDO/18/1801/2016/01038: ACRHEM-PHASE-III). Ganapathy Vaitheeswaran acknowledges the CMSD University of Hyderabad for providing the computational facilities, and expresses gratitude to the Institute of Eminence, University of Hyderabad (UOH-IOE-RC3-21-046), for their financial assistance.

References

- 1. Xie, W.; Koyama, M., Theoretical design of a technetium-like alloy and its catalytic properties. *Chemical Science* **2019**, *10* (21), 5461-5469.
- 2. Skomurski, F. N.; Rosso, K. M.; Krupka, K. M.; McGrail, B. P., Technetium incorporation into hematite (α-Fe₂O₃). *Environmental science & technology* **2010**, *44* (15), 5855-5861.
- 3. Meyer, R.; Arnold, W.; Case, F.; O'Kelley, G., Solubilities of Tc (IV) oxides. *Radiochimica Acta* **1991,** *55* (1), 11-18.
- 4. Lieser, K.; Bauscher, C., Technetium in the Hydrosphere and in the Geosphere. *Radiochimica Acta* **1987**, *42* (4), 205-214.
- 5. Taylor, C. D., Surface segregation and adsorption effects of iron–technetium alloys from first-principles. *Journal of nuclear materials* **2011**, *408* (2), 183-187.

- 6. Keiser Jr, D.; Abraham, D.; Richardson Jr, J., Influence of technetium on the microstructure of a stainless steel–zirconium alloy. *Journal of nuclear materials* **2000**, *277* (2-3), 333-338.
- 7. Burton-Pye, B. P.; Radivojevic, I.; McGregor, D.; Mbomekalle, I. M.; Lukens Jr, W. W.; Francesconi, L. C., Photoreduction of ⁹⁹Tc pertechnetate by nanometer-sized metal oxides: new strategies for formation and sequestration of low-valent technetium. *Journal of the American Chemical Society* **2011**, *133* (46), 18802-18815.
- 8. Pegg, I. L., Behavior of technetium in nuclear waste vitrification processes. *Journal of radioanalytical and nuclear chemistry* **2015,** *305*, 287-292.
- 9. Jin, T.; Kim, D.; Tucker, A. E.; Schweiger, M. J.; Kruger, A. A., Reactions during melting of low-activity waste glasses and their effects on the retention of rhenium as a surrogate for technetium-99. *Journal of Non-Crystalline Solids* **2015**, *425*, 28-45.
- 10. Kang, K.; Shen, N.; Wang, Y.; Li, L.; Zhang, M.; Zhang, X.; Lei, L.; Miao, X.; Wang, S.; Xiao, C., Efficient sequestration of radioactive ⁹⁹TcO₄- by a rare 3-fold interlocking cationic metalorganic framework: A combined batch experiments, pair distribution function, and crystallographic investigation. *Chemical Engineering Journal* **2022**, *427*, 130942.
- 11. Hu, Q.-H.; Shi, Y.-Z.; Gao, X.; Zhang, L.; Liang, R.-P.; Qiu, J.-D., An alkali-resistant metalorganic framework as halogen bond donor for efficient and selective removing of ReO_4^-/TcO_4^- . *Environmental Science and Pollution Research* **2022**, *29* (57), 86815-86824.
- 12. Dickson, J. O.; Harsh, J. B.; Lukens, W. W.; Pierce, E. M., Perrhenate incorporation into binary mixed sodalites: The role of anion size and implications for technetium-99 sequestration. *Chemical Geology* **2015**, *395*, 138-143.
- 13. Favre-Réguillon, A.; Draye, M.; Cote, G.; Czerwinsky, K. R., Insights in uranium extraction from spent nuclear fuels using dicyclohexano-18-crown-6 Fate of rhenium as technetium homolog. *Separation and Purification Technology* **2019**, *209*, 338-342.
- 14. Fei, H.; Bresler, M. R.; Oliver, S. R., A new paradigm for anion trapping in high capacity and selectivity: crystal-to-crystal transformation of cationic materials. *Journal of the American Chemical Society* **2011**, *133* (29), 11110-11113.
- 15. McCloy, J. S.; Riley, B. J.; Goel, A.; Liezers, M.; Schweiger, M. J.; Rodriguez, C. P.; Hrma, P.; Kim, D.-S.; Lukens, W. W.; Kruger, A. A., Rhenium solubility in borosilicate nuclear waste glass: Implications for the processing and immobilization of technetium-99. *Environmental Science & Technology* **2012**, *46* (22), 12616-12622.
- 16. Strub, E.; Grödler, D.; Zaratti, D.; Yong, C.; Dünnebier, L.; Bazhenova, S.; Roca Jungfer, M.; Breugst, M.; Zegke, M., Pertechnetates A structural study across the Periodic Table. *Chemistry A European Journal* **2024**, *30* (26), e202400131.
- 17. Shannon, R. D., Revised effective ionic radii and systematic studies of interatomic distances in halides and chalcogenides. *Acta Crystallographica Section A: Crystal Physics, Diffraction, Theoretical and General Crystallography* **1976**, *32* (5), 751-767.
- 18. Lukens, W. W.; McKeown, D. A.; Buechele, A. C.; Muller, I. S.; Shuh, D. K.; Pegg, I. L., Dissimilar behavior of technetium and rhenium in borosilicate waste glass as determined by X-ray absorption spectroscopy. *Chemistry of Materials* **2007**, *19* (3), 559-566.
- 19. Gan, H.; McKeown, D. A.; Xie, X.; Pegg, I. L., Assessment of rhenium as a surrogate for technetium in Hanford low activity waste borosilicate glasses: Speciation, solubility, and redox effects. *International Journal of Applied Glass Science* **2023**, *14* (1), 97-112.
- 20. Avdeev, M.; Thorogood, G. J.; Carter, M. L.; Kennedy, B. J.; Ting, J.; Singh, D. J.; Wallwork, K. S., Antiferromagnetism in a technetium oxide. Structure of CaTcO₃. *Journal of the American Chemical Society* **2011**, *133* (6), 1654-1657.
- 21. Rodriguez, E. E.; Poineau, F.; Llobet, A.; Kennedy, B. J.; Avdeev, M.; Thorogood, G. J.; Carter, M. L.; Seshadri, R.; Singh, D. J.; Cheetham, A. K., High temperature magnetic ordering in the 4*d* perovskite SrTcO₃. *Physical Review Letters* **2011**, *106* (6), 067201.

- 22. Thorogood, G. J.; Avdeev, M.; Carter, M. L.; Kennedy, B. J.; Ting, J.; Wallwork, K. S., Structural phase transitions and magnetic order in SrTcO₃. *Dalton Transactions* **2011**, *40* (27), 7228-7233.
- 23. Reynolds, E. M.; Yu, M.; Thorogood, G. J.; Brand, H. E.; Poineau, F.; Kennedy, B. J., Thermal expansion of ammonium pertechnetate and ammonium perrhenate. *Journal of Solid State Chemistry* **2019**, *274*, 64-68.
- 24. Saura-Múzquiz, M.; Mullens, B. G.; Maynard-Casely, H. E.; Kennedy, B. J., Neutron diffraction study of the monoclinic-tetragonal phase transition in NdNbO₄ and NdTaO₄. *Dalton Transactions* **2021**, *50*, 11485-11497.
- 25. Amarasinghe, D. K.; Perera, S. S.; Rabuffetti, F. A., Rotational disorder in scheelite-type $NaRE(MO_4)_2$ (RE = Rare-Earth, Y; M = Mo, W). Crystal Growth & Design **2020**, 20 (5), 3442-3448.
- 26. Boyd, G., Technetium and promethium. *Journal of Chemical Education* **1959**, *36*, 1-14.
- 27. Krebs, B.; Hasse, K.-D., Refinements of the crystal structures of KTcO₄, KReO₄ and OsO₄. The bond lengths in tetrahedral oxoanions and oxides of *d*⁰ transition metals. *Acta Crystallographica Section B: Structural Crystallography and Crystal Chemistry* **1976**, *32* (5), 1334-1337.
- 28. McDonald, B.; Tyson, G., The crystal structure of caesium, ammonium and potassium pertechnetates. *Acta Crystallographica* **1962**, *15* (1), 87-87.
- 29. Faggiani, R.; Gillespie, R.; Lock, C.; Pocé, J., The structure of ammonium pertechnetate at 295, 208 and 141 K. *Acta Crystallographica Section B: Structural Crystallography and Crystal Chemistry* **1980,** *36* (2), 231-233.
- 30. Weaver, J.; Soderquist, C. Z.; Washton, N. M.; Lipton, A. S.; Gassman, P. L.; Lukens, W. W.; Kruger, A. A.; Wall, N. A.; McCloy, J. S., Chemical trends in solid alkali pertechnetates. *Inorganic Chemistry* **2017**, *56* (5), 2533-2544.
- 31. Kanellakopulos, B., Zur kenntnis der hochtemperaturmodifikation einiger verbindungen des typs $Me^{1}XO_{4}$ (Me = Cs, Tl; X = Re, Tc, Cl). Journal of Inorganic and Nuclear Chemistry **1966**, 28 (3), 813-816.
- 32. Chay, C.; Avdeev, M.; Brand, H. E.; Injac, S.; Whittle, T. A.; Kennedy, B. J., Crystal structures and phase transition behaviour in the 5d transition metal oxides $AReO_4$ (A = Ag, Na, K, Rb, Cs and Tl). Dalton Transactions **2019**, 48 (47), 17524-17532.
- 33. Kennedy, B. J.; Injac, S.; Thorogood, G. J.; Brand, H. E.; Poineau, F., Structures and phase transitions in pertechnetates. *Inorganic Chemistry* **2019**, *58* (15), 10119-10128.
- 34. Marlton, F. P.; Mullens, B. G.; Chater, P. A.; Kennedy, B. J., Tetrahedral displacive disorder in the scheelite-type oxide RbReO₄. *Inorganic Chemistry* **2022**, *61* (38), 15130-15137.
- 35. Bastide, J., Simplified systematics of the compounds ABX_4 ($X = O^2$ -, F-) and possible evolution of their crystal-structures under pressure. *Journal of Solid State Chemistry* **1987**, 71 (1), 115-120.
- 36. Mullens, B. G.; Marlton, F. P.; Saura-Múzquiz, M.; Chater, P. A.; Kennedy, B. J., Tetrahedra rotational and displacive disorder in the scheelite-type oxide CsReO₄. *Inorganic Chemistry* **2024**, *63* (22), 10386-10396.
- 37. Romero-Vázquez, P. B.; López-Moreno, S.; Errandonea, D., First-principles study of *A*TcO₄ pertechnetates. *Journal of Physics and Chemistry of Solids* **2022**, *171*, 110979.
- 38. Mullens, B. G.; Avdeev, M.; Brand, H. E. A.; Mondal, S.; Vaitheeswaran, G.; Kennedy, B. J., Insights into the structural variations in SmNb_{1-x}Ta_xO₄ and HoNb_{1-x}Ta_xO₄ combined experimental and computational studies. *Dalton Transactions* **2021**, *50*, 9103-9117.
- 39. Mullens, B. G.; Saura-Múzquiz, M.; Marlton, F. P.; Avdeev, M.; Brand, H. E.; Mondal, S.; Vaitheeswaran, G.; Kennedy, B. J., Beyond the ionic radii: A multifaceted approach to understand differences between the structures of *LnNbO*₄ and *LnTaO*₄ fergusonites. *Journal of Alloys and Compounds* **2022**, *930*, 167399.
- 40. Nyman, M.; Rodriguez, M. A.; Rohwer, L. E.; Martin, J. E.; Waller, M.; Osterloh, F. E., Unique LaTaO₄ polymorph for multiple energy applications. *Chemistry of Materials* **2009**, *21* (19), 4731-4737.

- 41. Hartenbach, I.; Lissner, F.; Nikelski, T.; Meier, S. F.; Müller-Bunz, H.; Schleid, T., Über oxotantalate der lanthanide des formeltyps MTaO₄ (M = La–Nd, Sm–Lu). Zeitschrift für anorganische und allgemeine Chemie **2005**, 631 (12), 2377-2382.
- 42. Siqueira, K. P.; Dias, A., Effect of the processing parameters on the crystalline structure of lanthanide orthotantalates. *Materials Research* **2014**, *17*, 167-173.
- 43. Cordrey, K. J.; Stanczyk, M.; Dixon, C. A.; Knight, K. S.; Gardner, J.; Morrison, F. D.; Lightfoot, P., Structural and dielectric studies of the phase behaviour of the topological ferroelectric La_{1-x}Nd_xTaO₄. *Dalton Transactions* **2015**, *44* (23), 10673-10680.
- 44. Rögner, P.; Range, K. J., The crystal structure of β -Thallium perrhenate. *Zeitschrift für anorganische und allgemeine Chemie* **1993**, *619* (6), 1017-1022.
- 45. Jayaraman, A.; Kourouklis, G.; Fleming, R.; Van Uitert, L., Temperature-induced phase transitions in TlReO₄: A Raman spectroscopic and X-ray diffraction study. *Physical Review B* **1988**, *37* (1), 664.
- 46. de Waal, D.; Kiefer, W., Raman Investigation of the Low Temperature Phase Transitions in Monoclinic TlReO₄. *Zeitschrift für anorganische und allgemeine Chemie* **2004**, *630* (1), 127-130.
- 47. Mondal, S.; Vaitheeswaran, G.; Kennedy, B. J.; Chay, C.; Injac, S.; Errandonea, D., Crystal structure and phase transition of TlReO₄: a combined experimental and theoretical study. *Journal of Physics: Condensed Matter* **2020**, *33* (6), 065403.
- 48. Saura-Múzquiz, M.; Marlton, F. P.; Mullens, B. G.; Manjón-Sanz, A. M.; Neuefeind, J. C.; Everett, M.; Brand, H. E. A.; Mondal, S.; Vaitheeswaran, G.; Kennedy, B. J., Understanding the Reentrant Phase Transition in a Non-magnetic Scheelite. *Journal of the American Chemical Society* **2022**, *144* (34), 15612-15621.
- 49. Huq, A.; Kirkham, M.; Peterson, P. F.; Hodges, J. P.; Whitfield, P. S.; Page, K.; Hügle, T.; Iverson, E. B.; Parizzi, A.; Rennich, G., POWGEN: rebuild of a third-generation powder diffractometer at the Spallation Neutron Source. *Journal of Applied Crystallography* **2019**, *52* (5), 1189-1201.
- 50. Coelho, A. A., TOPAS and TOPAS-Academic: An optimization program integrating computer algebra and crystallographic objects written in C++. *Journal of Applied Crystallography* **2018**, *51* (1), 210-218.
- 51. Tucker, M., G.; Keen, D., A.; Dove, M., T.; Goodwin, A., L.; Hui, Q., RMCProfile: Reverse Monte Carlo for polycrystalline materials. *Journal of Physics: Condensed Matter* **2007**, *19* (33), 335218.
- 52. Momma, K.; Izumi, F., VESTA 3 for three-dimensional visualization of crystal, volumetric and morphology data. *Journal of Applied Crystallography* **2011**, *44* (6), 1272-1276.
- 53. Blöchl, P. E., Projector augmented-wave method. *Physical Review B* **1994,** *50* (24), 17953-17979.
- 54. Kresse, G.; Furthmüller, J., Efficient iterative schemes for ab initio total-energy calculations using a plane-wave basis set. *Physical Review B* **1996**, *54* (16), 11169-11186.
- 55. Armiento, R.; Mattsson, A. E., Functional designed to include surface effects in self-consistent density functional theory. *Physical Review B* **2005**, *72* (8), 085108.
- 56. Perdew, J. P.; Burke, K.; Ernzerhof, M., Generalized gradient approximation made simple. *Physical Review Letters* **1996,** *77* (18), 3865-3868.
- 57. Perdew, J. P.; Ruzsinszky, A.; Csonka, G. I.; Vydrov, O. A.; Scuseria, G. E.; Constantin, L. A.; Zhou, X.; Burke, K., Restoring the density-gradient expansion for exchange in solids and surfaces. *Physical Review Letters* **2008**, *100* (13), 136406.
- 58. Monkhorst, H. J.; Pack, J. D., Special points for Brillouin-zone integrations. *Physical Review B* **1976,** *13* (12), 5188-5192.
- 59. Koller, D.; Tran, F.; Blaha, P., Merits and limits of the modified Becke-Johnson exchange potential. *Physical Review B* **2011**, *83* (19), 195134.

- 60. Koller, D.; Tran, F.; Blaha, P., Improving the modified Becke-Johnson exchange potential. *Physical Review B* **2012**, *85* (15), 155109.
- 61. Singh, D. J., Electronic structure calculations with the Tran-Blaha modified Becke-Johnson density functional. *Physical Review B* **2010**, *82* (20), 205102.
- 62. Tran, F.; Blaha, P., Accurate band gaps of semiconductors and insulators with a semilocal exchange-correlation potential. *Physical Review Letters* **2009**, *102* (22), 226401.
- 63. Injac, S.; Yuen, A. K.; Avdeev, M.; Wang, C.-H.; Turner, P.; Brand, H. E.; Kennedy, B. J., Structural and magnetic studies of *ABO*₄-type ruthenium and osmium oxides. *Inorganic Chemistry* **2020**, *59* (5), 2791-2802.
- 64. Mullens, B. G.; Saura-Múzquiz, M.; Cordaro, G.; Marlton, F. P.; Maynard-Casely, H. E.; Zhang, Z.; Baldinozzi, G.; Kennedy, B. J., Variable temperature *in situ* neutron powder diffraction and conductivity studies of undoped HoNbO₄ and HoTaO₄. *Chemistry of Materials* **2024**, *36* (10), 5002-5016.
- 65. Sánchez-Martín, J.; Errandonea, D.; Pellicer-Porres, J.; Vázquez-Socorro, D.; Martínez-García, D.; Achary, S. N.; Popescu, C., Phase transitions of BiVO₄ under high pressure and high temperature. *The Journal of Physical Chemistry C* **2022**, *126* (17), 7755-7763.
- 66. Saura-Múzquiz, M.; Mullens, B. G.; Avdeev, M.; Jharapla, P. K.; Vaitheeswaran, G.; Gupta, M.; Mittal, R.; Kennedy, B. J., Experimental and computational insights into the anomalous thermal expansion of (NH₄)ReO₄. *Journal of Solid State Chemistry* **2022**, *315*, 123531.
- 67. Culver, S. P.; Brutchey, R. L., Thermally activated rotational disorder in CaMoO₄ nanocrystals. *CrystEngComm* **2016**, *18* (24), 4485-4488.
- 68. Rabuffetti, F. A.; Culver, S. P.; Suescun, L.; Brutchey, R. L., Structural disorder in *A*MoO₄ (*A* = Ca, Sr, Ba) scheelite nanocrystals. *Inorganic Chemistry* **2014**, *53* (2), 1056-1061.
- 69. Božin, E. S.; Malliakas, C. D.; Souvatzis, P.; Proffen, T.; Spaldin, N. A.; Kanatzidis, M. G.; Billinge, S. J., Entropically stabilized local dipole formation in lead chalcogenides. *Science* **2010**, *330* (6011), 1660-1663.
- 70. Knox, K.; Bozin, E.; Malliakas, C.; Kanatzidis, M.; Billinge, S., Local off-centering symmetry breaking in the high-temperature regime of SnTe. *Physical Review B* **2014**, *89* (1), 014102.
- 71. Laurita, G.; Seshadri, R., Chemistry, structure, and function of lone pairs in extended solids. *Accounts of Chemical Research* **2022**, *55* (7), 1004-1014.
- 72. Mullens, B. G.; Marlton, F. P.; Nicholas, M. K.; Permana, A. J.; Avdeev, M.; Mukherjee, S.; Vaitheeswaran, G.; Li, C.; Liu, J.; Chater, P. A.; Kennedy, B. J., Seeing the unseen: The structural influence of the lone pair electrons in PbWO₄. *Inorganic Chemistry* **2024**, *63* (24), 11176-11186.
- 73. Liu, T.; Zhang, X.; Guan, J.; Catlow, C. R. A.; Walsh, A.; Sokol, A. A.; Buckeridge, J., Insight into the fergusonite–scheelite phase transition of *ABO*₄-type oxides by density functional theory: A case study of the subtleties of the ground state of BiVO₄. *Chemistry of Materials* **2022**, *34* (12), 5334-5343.
- 74. Walsh, A.; Payne, D. J.; Egdell, R. G.; Watson, G. W., Stereochemistry of post-transition metal oxides: Revision of the classical lone pair model. *Chemical Society Reviews* **2011**, *40* (9), 4455-4463.
- 75. Walsh, A.; Yan, Y.; Huda, M. N.; Al-Jassim, M. M.; Wei, S.-H., Band edge electronic structure of BiVO₄: Elucidating the role of the Bi s and V d orbitals. *Chemistry of Materials* **2009**, *21* (3), 547-551.
- 76. Sleight, A. W.; Chen, H. Y.; Ferretti, A.; Cox, D. E., Crystal growth and structure of BiVO₄. *Materials Research Bulletin* **1979**, *14* (12), 1571-1581.
- 77. Subramanian, M.; Calabrese, J., Crystal structure of the low temperature form of bismuth niobium oxide [α -BiNbO₄]. *Materials Research Bulletin* **1993**, *28* (6), 523-529.
- 78. Zhuk, N.; Krzhizhanovskaya, M.; Belyy, V.; Sekushin, N.; Chichineva, A., The bismuth orthotantalate with high anisotropic thermal expansion. *Scripta Materialia* **2019**, *173*, 6-10.

- 79. Zhou, D.; Pang, L.-X.; Wang, H.; Yao, X., Phase composition and phase transformation in Bi(Sb,Nb,Ta)O₄ system. *Solid State Sciences* **2009**, *11* (11), 1894-1897.
- 80. Saura-Múzquiz, M.; Marlton, F. P.; Mullens, B. G.; Liu, J.; Vogt, T.; Maynard-Casely, H. E.; Avdeev, M.; Blom, D. A.; Kennedy, B. J., Cation and lone pair order–disorder in the polymorphic mixed metal bismuth scheelite Bi₃FeMo₂O₁₂. *Chemistry of Materials* **2023**, *35* (1), 123-135.

The data supporting this article have been included as part of the Supplementary Information.